nature communications

Article

https://doi.org/10.1038/s41467-025-59106-5

Structural plasticity of the FOXO-DBD:p53-TAD interaction

Received: 22 April 2024

Accepted: 4 December 2024

Published online: 27 May 2025

Check for updates

Klara Kohoutova[1,2], Pavel Srb[3], Veronika Obsilova[2] ✉, Vaclav Veverka[3,4] ✉ & Tomas Obsil[1,2] ✉

The transcription factors FOXO4 and p53 regulate aging, and their deregulation has been linked to several diseases, including cancer. Under stress conditions, cellular senescence is promoted by p53 sequestration and senescence-associated protein p21 transcriptional upregulation induced by interactions between the FOXO4 Forkhead DNA-binding domain and the p53 transactivation domain. However, the molecular details of these interactions remain unclear. Here, we report that these interactions between p53 and FOXO4 domains are highly heterogeneous. The p53 transactivation domain primarily interacts with the region formed by the N-terminal helical bundle of the FOXO4 Forkhead domain but retains a substantial degree of flexibility in the complex. In addition, NMR data-driven molecular simulations suggest that p53 interacts with FOXO4 through multiple binding modes. Overall, our findings not only provide the structural insights into interactions between FOXO4 and p53 but also highlight their potential as targets for developing senolytic compounds.

Cellular senescence entails two key cellular phenotypes, namely permanent cell cycle arrest and the senescent secretory phenotype, i.e., the secretion of interleukins, inflammatory cytokines, and growth factors[1]. Senescence can be induced by several factors, such as telomere loss, oxidative stress, and intense oncogenic signaling through cyclin-dependent kinase inhibitor (CDKI) p21 expression[2,3]. p21 expression is regulated by direct interactions between the transcription factors FOXO4 and p53, thereby suppressing apoptosis in senescent cells[4]. Accordingly, inhibiting this interaction disrupts p21 transcription, excludes active p53 from the nucleus, and induces senescent cell death.

FOXO (FOXO1, FOXO3, FOXO4, and FOXO6) proteins regulate various cellular functions, such as cell growth, survival, metabolism, and response to oxidative stress, by controlling the transcription of target genes when binding to consensus recognition motifs known as the Daf-16 family member-binding (DBE) and the insulin-responsive (IRE) elements[5,6]. All FOXO proteins have a similar domain structure with a highly conserved Forkhead DNA-binding domain (DBD) and a C-terminal transactivation domain (Supplementary Fig. S1a, b)[7,8]. In all FOXO proteins, FOXO-DBD is flanked by intrinsically disordered N- and C-terminal segments that modulate their transcriptional activity. For example, FOXO4 phosphorylation by c-Jun N-terminal kinase (JNK) upregulates p21 and thus activates cellular senescence, whereas FOXO1 and FOXO3 inhibit senescence[9–11]. These antagonistic roles of FOXO family members in regulating senescence may be explained by JNK phosphorylation of two residues (T447 and T451) in the unstructured C-terminal segment of FOXO4 in response to oxidative stress as FOXO3 and FOXO1 lack these phosphorylation sites[9,12].

The transcription factor p53 regulates a wide range of cellular processes, including metabolic adaptation, DNA repair, cell cycle arrest, apoptosis, and senescence. These diverse functions of p53 are related to its multidomain architecture, which allows various inter- and intramolecular interactions[13]. p53 consists of an N-terminal transactivation domain (TAD, residues 1–61), a proline-rich domain (PRD,

[1]Department of Physical and Macromolecular Chemistry, Faculty of Science, Charles University, Prague, Czech Republic. [2]Institute of Physiology of the Czech Academy of Sciences, Laboratory of Structural Biology of Signaling Proteins, Division BIOCEV, Vestec, Czech Republic. [3]Institute of Organic Chemistry and Biochemistry of the Czech Academy of Sciences, Prague, Czech Republic. [4]Department of Cell Biology, Faculty of Science, Charles University, Prague, Czech Republic. ✉e-mail: veronika.obsilova@fgu.cas.cz; vaclav.veverka@uochb.cas.cz; obsil@natur.cuni.cz

residues 62–92), a DNA-binding domain (DBD, residues 93-293), a tetramerization domain (TD, residues 325-355) and a C-terminal negative regulatory domain (NRD, residues 367–393)[14]. Among these domains, p53-TAD stands out for its intrinsically disordered structure containing two acidic regions, namely TAD1 (residues 17–29) and TAD2 (residues 40–57) (Supplementary Fig. S1c). Moreover, the conserved hydrophobic residues F19, L22, W23, L25, L26, I50, W53, and F54 of these regions play a key role in gene transactivation due to their involvement in protein-protein interactions[15–19]. Case in point, p53-TAD mediates the interaction of p53 with a number of its binding partners, such as the transcription factor IID complex[16], a key negative regulator of the E3 ubiquitin-protein ligase mouse double minute 2 homolog (MDM2)[20], and the histone acetyltransferase paralogs CREB-binding protein (CBP) and p300, which are important for p53-mediated transactivation[17,18,21]. In response to ionizing radiation-induced DNA damage, p53-TAD protein-protein interactions are modulated by phosphorylation at several residues (S6, S9, S15, T18, S20, S33, S37, S46 and T55) by several kinases, including casein kinase 1 (CK1), ataxia-telangiectasia mutated (ATM) protein kinase, p38 kinase, extracellular signal-regulated kinase (ERK), transcription initiation factor TFIID subunit 1 (TAF1) kinase and DNA-dependent protein kinase (DNA-PK)[18,22–25].

Interactions between FOXO transcription factors and p53 were first described by Nemoto et al.[26], who reported that FOXO3 co-immunoprecipitated with p53 expressed both recombinantly and in human HELA cell lines. In subsequent structural studies, some authors have found that the Forkhead DBD and C-terminal TAD of FOXO3 contributed to its interactions with p53, proposing that p53-DBD suffices to form the FOXO3:p53 complex[27]. But we[28] and other authors[29] have argued that the FOXO4:p53 complex formation (i) requires the DBD of both proteins and (ii) is primarily mediated by the interaction between the N-terminal portion of FOXO4-DBD and the TAD2 region of p53-TAD, which forms the binding interface. As a result, the exact mechanism whereby FOXO4 interacts with p53 and upregulates p21 transcription remains unclear. Moreover, individual FOXO proteins likely interact with p53 through different mechanisms.

Considering the above, further structural studies must be conducted to characterize the interactions between FOXO4-DBD and p53-TAD. However, these interactions are transient, as evidenced by the rapid or intermediate exchange in ^{1}H-^{15}N heteronuclear single quantum coherence (HSQC) spectra[28,29]. Such transient interactions preclude the use of standard NMR techniques, hampering efforts to perform a detailed structural analysis of this complex. Nevertheless, the structure of this complex may be characterized using an approach based on paramagnetic relaxation enhancement (PRE) NMR measurements. This approach is a suitable alternative for studying systems in which standard structural biology methods cannot be applied[30], as shown by the structure of the ternary nuclear export complex[31], the mini-chromosome maintenance complex of *Sulfolobus solfataricus*[32] and the complex between the FusB fusidic acid resistance protein and a fragment of elongation factor G lacking N-terminal domains[33].

Here, we aimed at structurally characterizing the FOXO4-DBD:p53-TAD complex using a hybrid approach based on PRE NMR and molecular modeling. For this purpose, we used PRE-based distance constraints as input data for molecular docking simulations, thereby constructing a more reliable structural model. Overall, our findings provide structural insights into interactions between p53-TAD and the Forkhead domain of FOXO4.

Results

FOXO-DBDs differ in their binding affinities to p53-TAD

FOXO4-DBD and p53-TAD interact with micromolar binding affinity[28,29]. FOXO proteins likely interact differently with p53-TAD considering the sequence variability of the N- and C-terminal segments of the FOXO Forkhead domain and the key role of these regions, particularly the N-terminal segment. Supporting this assumption, our ^{1}H-^{15}N HSQC titration experiments with ^{15}N-labeled FOXO1-DBD (residues 144–270), FOXO3-DBD (residues 142–267) and FOXO4-DBD (residues 86–211) and unlabeled full-length p53-TAD (residues 1–93) showed subtle differences in their binding patterns (Fig. 1a, b and Supplementary Figs. 2–4). In the analysis of ^{1}H and ^{15}N chemical shift perturbations (CSP) of the amide groups of individual FOXO-DBDs, we found the largest changes in the N-terminal region of DBDs, especially in residues N99, W101 (FOXO4 numbering) of the N-terminal segment, in residues G102, N103, S105 of the helix H1 and in residues V135, Y137, F138 of the region between helices H2 and H4 for all three FOXO proteins.

Titration experiments with ^{15}N-labeled p53-TAD and unlabeled FOXO-DBDs showed similar but not identical distributions of CSPs. The most affected region of p53-TAD was the TAD2 region with residues M40, D42, L43, L45, S46, D48, I50, Q52, W53 and T55 (Fig. 1c, d and Supplementary Figs. 5–7). These results are in line with previous reports, according to which the N-terminal segment of FOXO4-DBD and the TAD2 region of p53 form a key part of the binding interface of the FOXO4:p53 complex[28,29].

In their interactions with p53-TAD, FOXO-DBDs primarily differ in the absolute range of CSP values assessed at the same concentrations, indicating significant differences in the binding affinity of FOXO-DBDs to p53-TAD (Fig. 1a–c). To assess differences in binding affinities, we performed fluorescence anisotropy (FA) measurements with FOXO-DBDs and 5-iodoacetoamidofluorescein (5-IAF)-labeled p53-TAD A63C mutant (Fig. 1e). To verify that the insertion of a fluorescein moiety into the p53-TAD molecule did not affect its interaction with FOXO4-DBD, the binding affinities of ^{15}N-labeled p53-TAD WT and the fluorescein-labeled ^{15}N-p53-TAD A63C mutant were compared based on concentration-dependent changes in CSPs. These measurements indicated that inserting a fluorescein moiety slightly increased the binding affinity of p53-TAD to FOXO4-DBD (Supplementary Fig. 8). Therefore, the K_D values from FA measurements should only be used to compare individual FOXO-DBD:p53-TAD complexes or p53-TAD mutants. FA measurements revealed that FOXO3-DBD binds to p53-TAD with higher affinity ($1.2 \pm 0.1\,\mu M$ K_D) than FOXO1- and FOXO4-DBD (8.8 ± 0.8 and $42 \pm 6\,\mu M$ K_D, respectively). Taken together, our ^{1}H-^{15}N HSQC NMR and FA assay data suggest that all three FOXO-DBDs bind to p53-TAD in a similar but not identical manner as reflected by their CSP profiles and different affinities.

Complex formation induces a more compact p53-TAD

^{1}H-^{15}N HSQC experiments with ^{15}N-labeled proteins revealed a fast exchange of free and bound FOXO4-DBD:p53-TAD complex on the NMR chemical shift timescale. Such a fast exchange precludes solution structure determination using standard NMR methods. To improve the stability of the complex, we designed two chimeric proteins, $FOXO4_{86\text{-}211}$-$(GGGGS)_2$-$p53_{1\text{-}93}$ and $p53_{1\text{-}93}$-$(GGGGS)_2$-$FOXO4_{86\text{-}211}$. However, we observed an intermediate exchange of free and bound complex in both chimeras, which still prevented us from solving the structure. Therefore, we combined PRE NMR experiments with molecular modeling to study the structure of the FOXO4-DBD:p53-TAD complex.

In PRE NMR, the presence of a paramagnetic probe increases the relaxation rate of the nearby ^{15}N-labeled NH groups, thereby reducing their intensity in the ^{1}H-^{15}N HSQC spectra[30]. In addition, the ^{1}H-Γ_2 relaxation rates can be used to calculate the intermolecular distances between the paramagnetic probe and the H_N atoms of ^{15}N-labeled NH groups[34]. For this purpose, three FOXO4-DBD and four p53-TAD single-Cys mutants were designed and subsequently covalently labeled with a paramagnetic MTSSL probe using thiol chemistry. In FOXO4-DBD, the single Cys residue was placed at positions 96 (mutation S96C) in the N-terminal segment, 134 (T134C) at the start of helix H4, and 162 (S162C) between helix H3 and β-strand S2 (Supplementary Fig. S1b).

https://doi.org/10.1038/s41467-025-59106-5

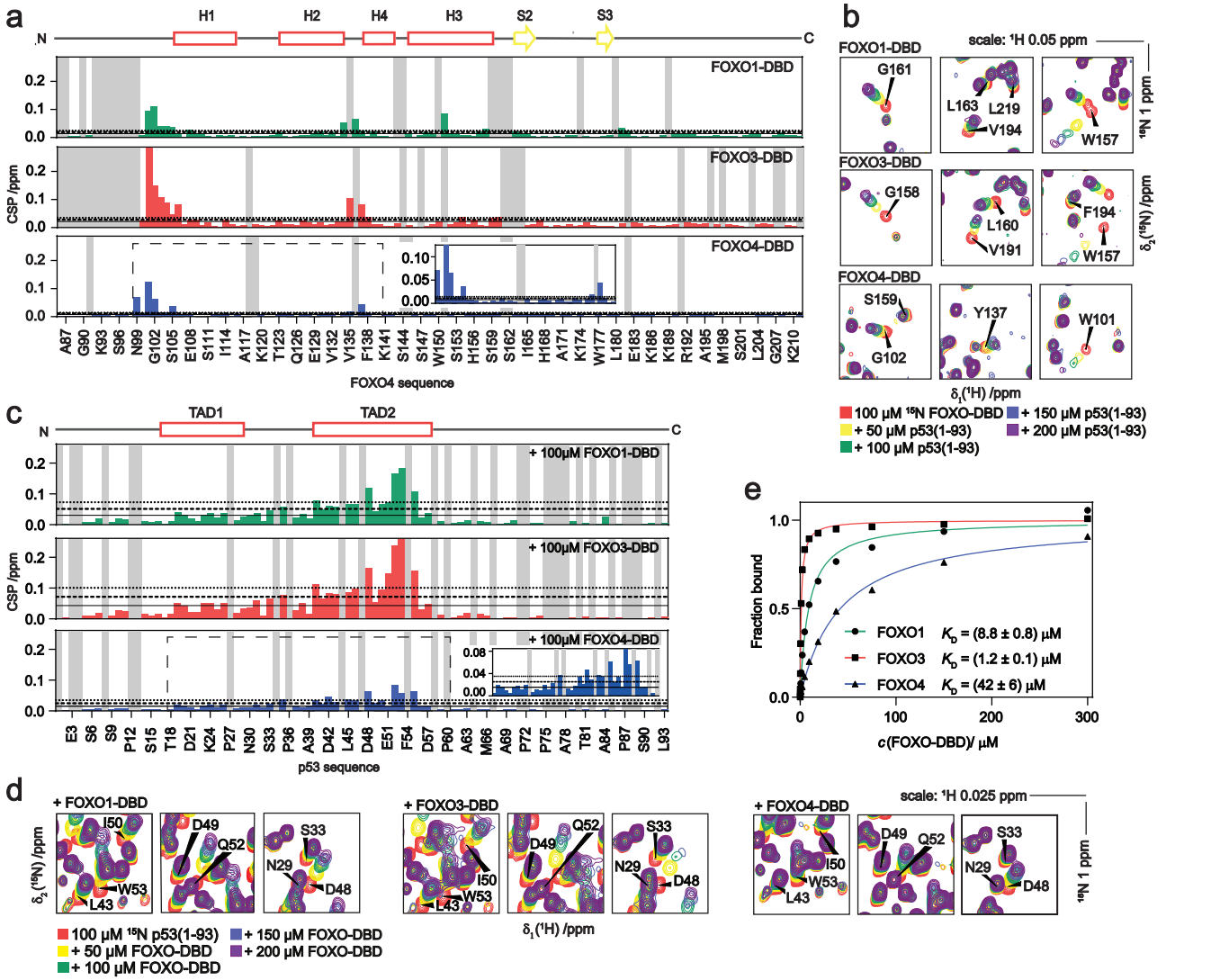

Fig. 1 | FOXO-DBDs bind to p53-TAD in the same manner but with different affinities. a Distribution of CSPs of 100 µM ^{15}N-labeled FOXO-DBDs with 100 µM p53-TAD. CSPs determined for ^{15}N-labeled FOXO1-DBD, FOXO3-DBD, and FOXO4-DBD with $p53_{TAD}$ at a molar ratio of 1:1 are shown in green, red, and blue, respectively. The gray bars correspond to residues with missing assignments in 2D ^{1}H-^{15}N HSQC spectra. The horizontal solid, dashed, and dotted lines correspond to the mean CSP value, the mean value + 1σ_{cor}, and the mean value + 2σ_{cor}, respectively. The inset shows the enlarged area of the CSP profile marked with a rectangle. **b** Detailed views of the selected peaks from ^{1}H-^{15}N HSQC spectra of ^{15}N-labeled FOXO-DBDs. **c** Distribution of CSPs of 100 µM ^{15}N-labeled p53-TAD. CSPs of ^{15}N-labeled p53-TAD with FOXO1-DBD, FOXO3-DBD, and FOXO4-DBD, at a molar ratio of 1:1, are shown in green, red, and blue, respectively. The gray bars correspond to residues with missing assignments in 2D ^{1}H-^{15}N HSQC spectra. The horizontal solid, dashed, and dotted lines correspond to the mean CSP value, the mean value + 1σ_{cor}, and the mean value + 2σ_{cor}, respectively. The inset shows the enlarged area of the CSP profile marked with a rectangle. **d** Detailed views of the selected peaks from ^{1}H-^{15}N HSQC spectra of ^{15}N-labeled p53-TAD. **e** 5-IAF-labeled p53-TAD A63C mutant binding to FOXO-DBDs. The binding affinities of FOXO-DBDs were determined by fitting FA data to a one-site binding model. Results are expressed as the mean of three technical replicates (n = 3).

p53-TAD was labeled at positions 15 (mutation S15C) at the start of TAD1, 37 (S37C) in the linker between TAD1 and TAD2, and 63 (A63C) and 90 (S90C) in the C-terminal region of p53-TAD (Supplementary Fig. 1c). The CSPs profiles of ^{15}N-labeled p53-TAD in the presence of MTSSL-labeled FOXO4-DBD mutants and of ^{15}N-labeled FOXO4-DBD in the presence of MTSSL-labeled p53-TAD mutants showed that attaching the paramagnetic label to selected positions in both proteins had no significant effect on their interaction (Supplementary Figs. 9 and 10).

To understand how the formation of this complex affects the conformation of FOXO4-DBD and p53-TAD, we first investigated potential changes in secondary structure upon complex formation. When analyzing the HN, HA, CA, CB, CO, and N chemical shifts of p53-TAD and FOXO4-DBD in their free and bound states (Supplementary Fig. 11), we concluded that complex formation did not induce any significant changes in the secondary structure of either protein. Subsequently, we performed intramolecular PRE NMR experiments with the MTSSL-labeled ^{15}N-FOXO4-DBD T134C mutant (both with and without unlabeled p53-TAD) and with the MTSSL-labeled ^{15}N-p53-TAD S15C mutant (both with and without unlabeled FOXO4-DBD). In our measurements with MTSSL-labeled ^{15}N-FOXO4-DBD T134C, we found no significant differences in intramolecular distances between the MTSSL moiety at position 134 and the H_N atoms of FOXO4-DBD in the free and bound states, with only a slight decrease in the I_{para}/I_{dia} intensity ratios of residues of the N-terminal segment (86-108) after p53-TAD binding (Supplementary Figs. 12 and 13). This result suggests that p53-TAD binding does not induce a significant conformational change in FOXO4-DBD other than a slight change in the position of the N-terminal segment.

https://doi.org/10.1038/s41467-025-59106-5

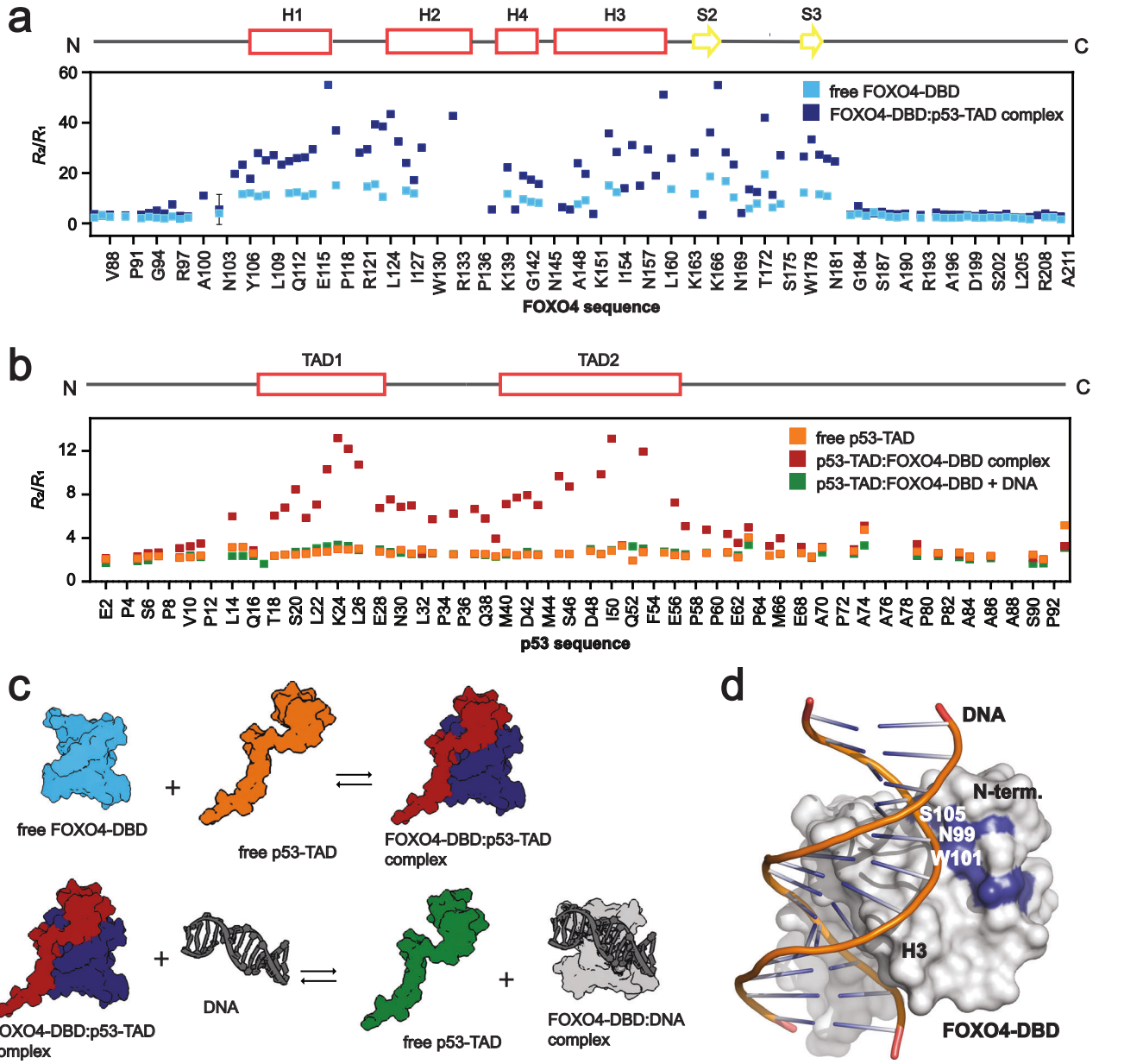

Fig. 2 | Interaction with FOXO4-DBD has little effect on p53-TAD flexibility. a R_2/R_1 ratios of ^{15}N-labeled FOXO4-DBD with and without p53-TAD (dark and light blue, respectively). **b** R_2/R_1 ratios of ^{15}N-labeled p53-TAD with and without FOXO4-DBD (red and orange, respectively). R_2/R_1 ratios of ^{15}N-labeled p53-TAD with FOXO4-DBD and dsDNA containing the DBE motif are shown in green. R_1 and R_2 relaxation rates were estimated by fitting the T_1 and T_2 peak intensities to a single exponential decay. The error in the relaxation rate was obtained from the error of the fit of the data. **c** Color coding for experiments shown in panels (**a** and **b**). **d** Overlap between p53- and DNA-binding surfaces of FOXO4-DBD. The residues with the largest CSPs in the ^{1}H-^{15}N HSQC spectrum of ^{15}N-labeled FOXO4-DBD after p53-TAD binding are shown in blue on the surface representation of the crystal structure of the FOXO4-DBD:DNA complex (PDB ID: 3L2C).

The PRE-based distances also matched those of the solution structure of FOXO4-DBD. In contrast, the I_{para}/I_{dia} intensity ratios of residues of both TAD1 and TAD2 regions (residues 18-59) of p53-TAD were considerably reduced in PRE NMR measurements with the MTSSL-labeled ^{15}N-p53-TAD S15C mutant (Supplementary Figs. 14 and 15). Accordingly, in the FOXO4-DBD:p53-TAD complex, this region of p53-TAD is closer to MTSSL at position 15, i.e., p53-TAD adopts a more compact conformation.

p53-TAD remains highly flexible upon complex formation

p53-TAD is an unstructured and highly flexible domain. To investigate how the conformation of p53-TAD and FOXO4-DBD changes during complex formation, relaxation measurements were performed with ^{15}N-labeled p53-TAD and FOXO4-DBD. The backbone flexibility was evaluated by measuring the ratio of the ^{15}N transverse (R_2) and longitudinal relaxation rates (R_1) of backbone amide nitrogen atoms, which decreases with the increase in internal dynamics. The resulting R_2/R_1 values showed that the N-terminal and C-terminal regions of FOXO4-DBD remain flexible, even upon complex formation ($R_2/R_1 < 10$), whereas its structured core (residues 100-185) is more rigid upon p53-TAD binding (Fig. 2a, c). In contrast, most of p53-TAD appears to remain highly flexible in the complex, with only TAD1 and TAD2 segments (residues 18–29 and 40–56, respectively) showing somewhat less flexibility (Fig. 2b, c). These findings corroborate previous observations that have identified these regions, particularly TAD2, as key components of the p53-binding surface of FOXO4[28,29].

https://doi.org/10.1038/s41467-025-59106-5

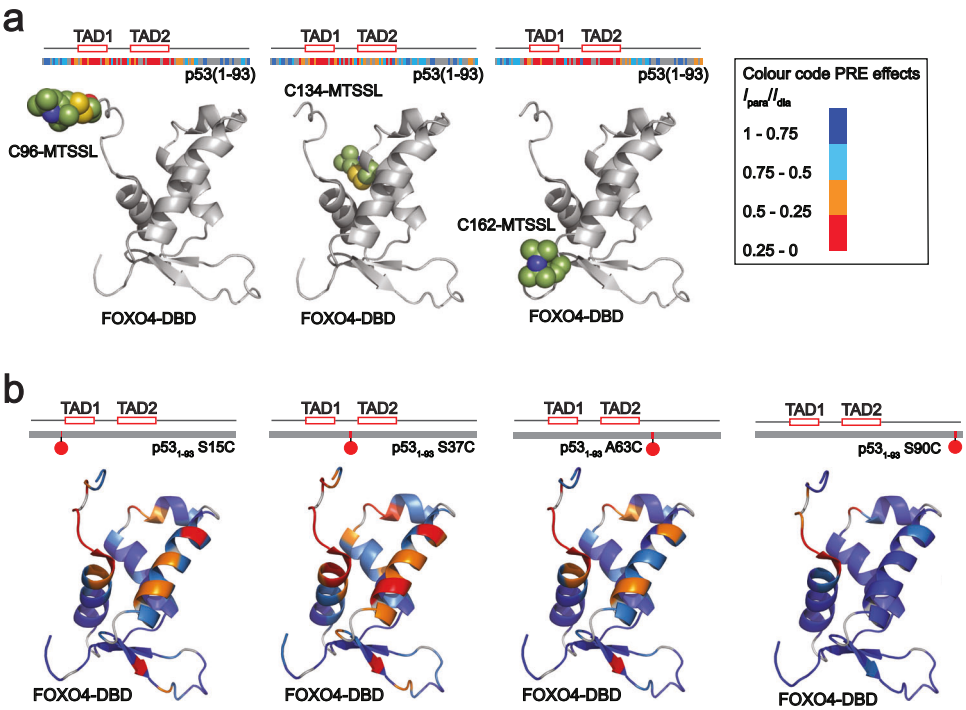

Fig. 3 | PRE NMR measurements. a PRE effect on the p53-TAD sequence; the color code of PRE effects is explained in captions. Residues with missing assignments in the 2D ^{1}H-^{15}N HSQC spectra are highlighted in gray. FOXO4-DBD structures (PDB ID: 1E17) show positions of the MTSSL moiety (highlighted in pale green). **b** PRE effects are shown on the solution structure of FOXO4-DBD (PDB ID: 1E17). The color code of PRE effects is explained in captions. Residues with missing assignments in 2D ^{1}H-^{15}N HSQC spectra are highlighted in gray. The position of the MTSSL moiety in p53-TAD is indicated by the red circle.

Because previous studies had also suggested that p53 interacts with several regions of the FOXO4-DBD involved in DNA binding, such as the N-terminal segment and the α-helix H3[28,29], we assessed whether FOXO4-DBD formed a ternary complex with p53-TAD and DNA. However, our ^{15}N relaxation measurements showed that p53-TAD displayed the same flexibility (values of the R_2/R_1 ratio) after adding equimolar amounts of DNA containing the DBE motif (sequence: 5′-GACTATG-TAAACAACGC-3′) to the FOXO4-DBD:p53-TAD complex as in the free state (Fig. 2b, c). This result indicates that the FOXO4-DBD:DNA complex formation is followed by p53-TAD dissociation and that the p53-TAD- and DNA-binding surfaces of FOXO4-DBD overlap with each other (Fig. 2d). The same effect, i.e., p53-TAD displacement by DNA binding, was also observed in FOXO1-DBD and FOXO3-DBD (Supplementary Fig. 16).

Modeling of the FOXO4-DBD:p53-TAD complex

Modeling the FOXO4-DBD:p53-TAD complex required calculating distance constraints between the two proteins from intermolecular PRE NMR measurements with 100 μM ^{15}N-labeled p53-TAD WT and 200 μM single-Cys MTSSL-labeled FOXO4-DBD mutants in both paramagnetic and diamagnetic states (Fig. 3a and Supplementary Figs. 17–20). These initial experiments revealed that the MTSSL probe at positions 96 and 162 of FOXO4-DBD induced a strong PRE effect on both TAD1 and TAD2, as indicated by the I_{para}/I_{dia} intensity ratios, which were lower than 0.25. Conversely, the probe at position 134 induced a strong effect on TAD1 (I_{para}/I_{dia} intensity ratios <0.25), but less so on TAD2 (I_{para}/I_{dia} intensity ratios < 0.75). Thus, the MTSSL probe attached at positions 96 and 162 of FOXO4-DBD is approximately equidistant from the p53 TAD1 and TAD2 regions, whereas the MTSSL at position 134 of FOXO4-DBD is closer to TAD1 than to TAD2.

We performed our subsequent intermolecular PRE NMR measurements using 100 μM ^{15}N-labeled FOXO4-DBD WT and 200 μM single-Cys MTSSL-labeled p53-TAD mutants in both paramagnetic and diamagnetic states (Fig. 3b and Supplementary Figs. 21–25). These experiments revealed that the MTSSL probes located at positions 15, 37, and 63 of the p53-TAD are very close to the N-terminal moiety of helix H1 of FOXO4-DBD (I_{para}/I_{dia} intensity ratios < 0.1). Furthermore, MTSSL at position 37 in the region between TAD1 and TAD2 is closer to the helix H3 and the C-terminal segment of FOXO4-DBD than in other p53-TAD mutants, but MTSSL at position 90, i.e., at the C-terminus of p53-TAD, has little effect on the intensity of FOXO4-DBD signals, except for residues from the N-terminal moiety of helix H1.

In total, 617 PRE-NMR-derived distances were used to model the structure of the FOXO4-DBD:p53-TAD complex using the HADDOCK program, as further detailed in Materials and Methods. The resulting model of the FOXO4-DBD:p53-TAD complex consists of a set of nine conformers (one is represented twice) selected for their agreement with experimental I_{para}/I_{dia} intensity ratios from PRE NMR measurements (Fig. 4, Supplementary Figs. 26–28 and Supplementary Data 2). This ensemble matches experimental CSP profiles (Figs. 1 and 4) and flexibility data derived from ^{15}N relaxation measurements, indicating that the central part of FOXO4-DBD (region 100–180) is rigid, while the N- and C-terminal segments are flexible (Fig. 2). This model suggests that the p53-TAD-binding surface of FOXO4-DBD is formed by the N-terminal segment (residues 86-106), the bend between helices H2 and H4, helix H3, and the C-terminal segment (residues 186–211). In addition, models of the FOXO4-DBD:p53-TAD complex, constructed either by HADDOCK simulation based on CSP analysis or by AlphaFold2, show a considerably lower agreement with experimental values of I_{para}/I_{dia} intensity ratios (Supplementary Figs. 29 and 30). This lower agreement confirms the importance of using distance constraints to obtain a reliable structural model for a dynamic system such as the FOXO4-DBD:p53-TAD complex.

As expected, the conformations of p53-TAD and both terminal segments of FOXO4-DBD is highly variable, in line with the results of our ^{15}N relaxation measurements (Fig. 2). The TAD2 region, which is located approximately in the middle of the p53-TAD construct and has

https://doi.org/10.1038/s41467-025-59106-5

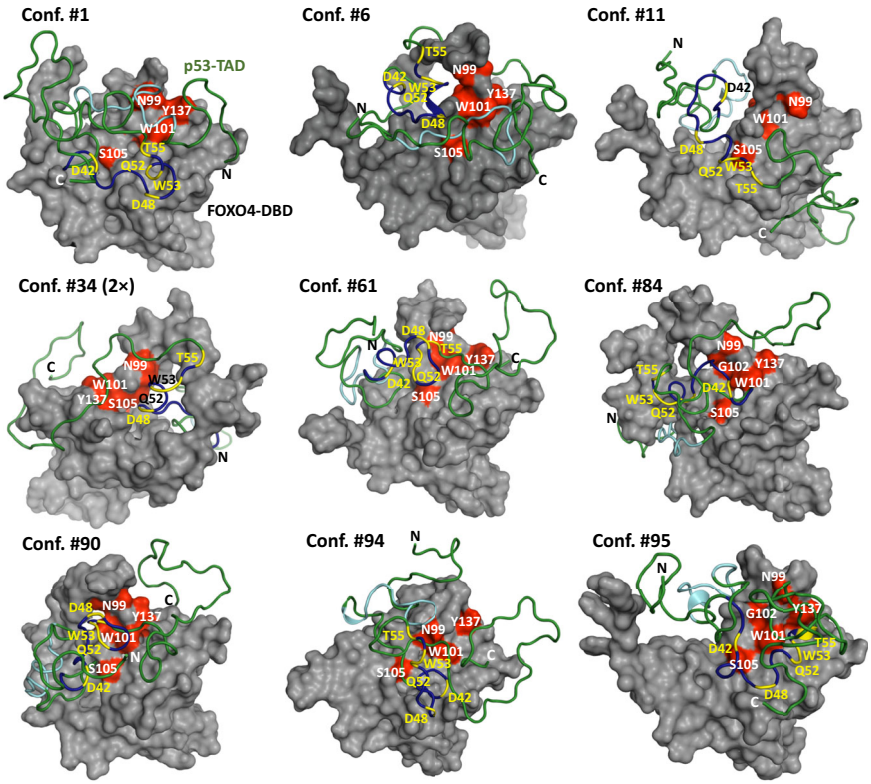

Fig. 4 | The HADDOCK model of the FOXO4-DBD:p53-TAD complex. The model of the FOXO4-DBD:p53-TAD complex consists of a set of ten conformers (conformer #34 is included twice) selected for their agreement with experimental I_{para}/I_{dia} intensity ratios from PRE measurements. FOXO4-DBD is shown as a gray surface, and the p53-TAD is shown as a green ribbon. The residues with the largest CSPs in ^{1}H-^{15}N HSQC spectra of FOXO4-DBD and p53-TAD are shown in red and yellow, respectively. The p53 TAD1 and TAD2 regions are highlighted in cyan and dark blue, respectively.

the highest CSP values, usually adopts a relatively compact conformation with a number of inter- and intramolecular interactions. Contact with FOXO4-DBD never involves the whole TAD2, and the remaining section of this region interacts with other parts of the p53-TAD. However, the pattern of individual interactions varies considerably from one conformer to another. The N-terminal region of FOXO4-DBD that precedes helix H1 and contains the residues with the most significant CSPs is always involved in interactions with p53-TAD (Fig. 4 and Supplementary Fig. 28). Furthermore, the C-terminal segment of FOXO4-DBD is also frequently involved in interactions with p53-TAD, even though no significant CSPs were observed in this region (Fig. 1a). This lack of significant CSPs is likely related to the high heterogeneity of interactions between FOXO4-DBD and p53-TAD. Based on the HADDOCK model of the FOXO4-DBD:p53-TAD complex, the interactions between p53-TAD and FOXO4-DBD are highly heterogeneous, and p53-TAD mainly interacts with the N-terminal region of FOXO4-DBD but remains highly flexible, nonetheless. Such interactions may explain both the relatively weak binding affinity (Fig. 1e) and the small number of FOXO4 residues affected by complex formation (Fig. 1a).

Hydrophobic residues of TAD help to maintain complex stability

Conserved hydrophobic residues, such as F19, L22, W23, L25, L26, I50, W53, and F54, are crucial for TAD1 and TAD2 function because they mediate interactions with several p53-TAD binding partners, as shown in previous studies[16–18,35]. To assess whether hydrophobic residues are also important for interactions between p53-TAD and FOXO4-DBD, we prepared ten p53-TAD single mutants and their combinations, namely F19A, W23A, W53A, F54A, F19A + W23A, L22A + L26A, V31A + L32A, W53A + F54A, F19A + W23A + W53A + F54A, and F19A + L22A + W23A + L26A + L31A + L32A + W53A + F54A. All mutants also contained the A63C mutation for their labeling with a fluorescent probe. Binding experiments based on fluorescence anisotropy measurements demonstrated that the F19A, W23A, F19A + W23A, L22A + L26A and V31A + L32A mutants interacted with FOXO4-DBD with a slightly higher binding affinity, that the W53A mutation had no effect and that the F54A, W53A + F54A, F19A + W23A + W53A + F54A and F19A + L22A + W23A + L26A + L31A + L32A + W53A + F54A mutants interacted with FOXO4-DBD with a significantly lower binding affinity than p53-TAD with only the A63C mutation (denoted as WT; Fig. 5a). Given the lack of a uniform binding interface between FOXO4-DBD and p53-TAD, indicated by the HADDOCK model, the reason for these changes in binding affinity remains unclear. Nevertheless, the mutated hydrophobic residues participate in both intramolecular and intermolecular contacts in the complex (Supplementary Fig. 31). In addition, residues W53 and F54 of TAD2 often form part of the binding interface, as suggested by conformers #6, 11, 61, 84, 90 and 95. Thus, these mutations might have affected both the conformational dynamics of p53-TAD and its interactions with FOXO4-DBD.

Phosphorylation of p53-TAD affects its affinity for FOXO4-DBD

The FOXO4-DBD and p53-TAD proteins are highly charged, as FOXO4-DBD is basic (theoretical pI 10.7) and p53-TAD is acidic (theoretical pI 3.47) (Supplementary Figs. 32 and 33). Therefore, electrostatic interactions should play a key role in complex formation. In line with this assumption, increasing the ionic strength significantly decreases the stability of the FOXO4-DBD:p53-TAD complex (Fig. 5b). In addition, the HADDOCK model of the FOXO4-DBD:p53-TAD complex suggested that the positively charged residues of the N- and C-termini of FOXO4-DBD (R92, K93, R97, R98, K189, R192-194, K203, R206, R208 and K210) are often close to the phosphorylation sites of p53-TAD (S15, T18, S20,

https://doi.org/10.1038/s41467-025-59106-5

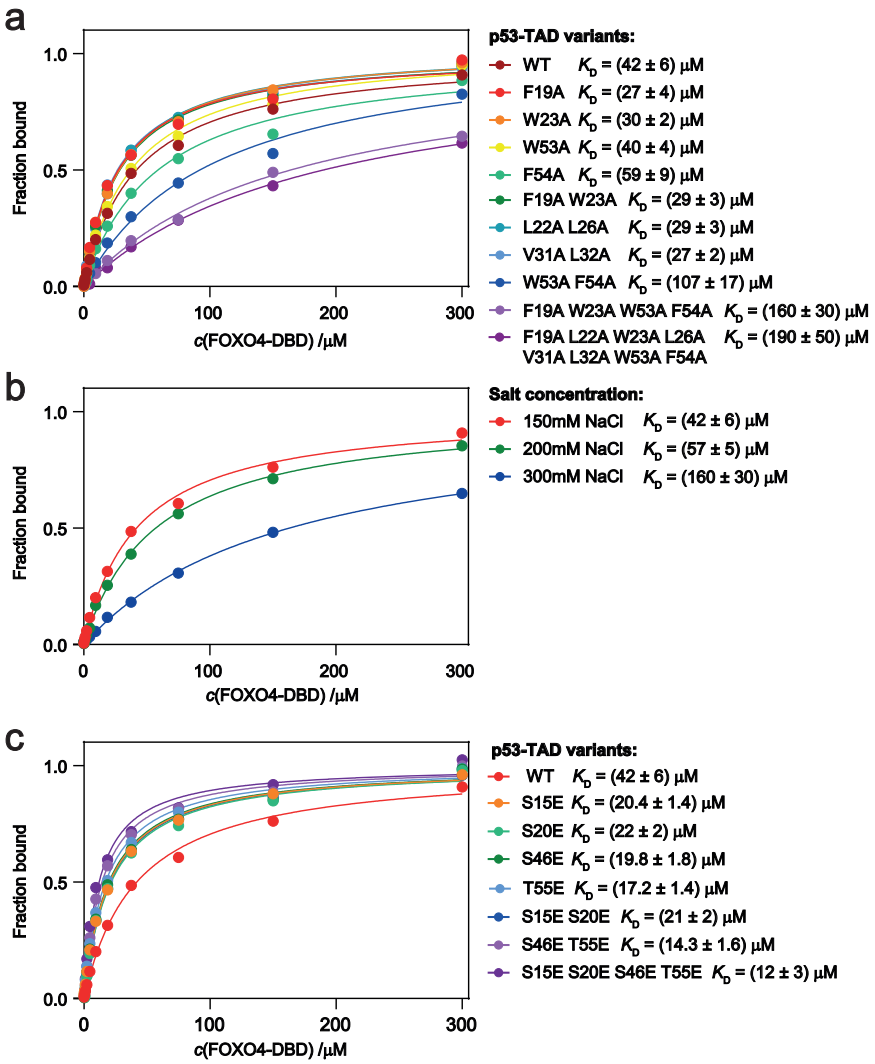

Fig. 5 | Hydrophobic and electrostatic interactions are critical for the formation of the FOXO4-DBD:p53-TAD complex. Binding of (**a**) 5-IAF-labeled p53-TAD WT and hydrophobic residues mutants to FOXO4-DBD, (**b**) 5-IAF-labeled p53-TAD WT to FOXO4-DBD at different salt concentrations, and (**c**) 5-IAF-labeled p53-TAD WT and phosphorylation-mimicking mutants to FOXO4-DBD. The binding affinities for FOXO4-DBD were determined by fitting FA data to a one-site binding model. Results are expressed as the mean of three technical replicates ($n = 3$).

S33, S37, S46 and T55) (Supplementary Fig. 34), which are targeted by different kinases in response to DNA damage or constitutively phosphorylated in unstressed cells[18,22,23]. Therefore, introducing a negative charge by phosphorylating these residues may significantly modulate p53-TAD interactions with positively charged surfaces of FOXO4-DBD.

To test this hypothesis, phosphorylation mimicking mutants of p53-TAD S15E, S20E, S46E, T55E, S15E + S20E, and S15E + S20E + S46E + T55E were prepared. FA measurements revealed that all phospho-mimicking p53-TAD mutants bind to FOXO4-DBD with higher affinity than p53-TAD WT. The S46E and T55E mutations in TAD2 had a slightly stronger effect than the S15E and S20E mutations in TAD1. The S46E + T55E and S15E + S20E + S46E + T55E mutants showed the highest binding affinities, with K_D values of 14.3 ± 1.6 and 12 ± 3 μM, respectively (Fig. 5c). In conclusion, p53-TAD phosphorylation increases its binding affinity for FOXO4-DBD.

Discussion

p53-TAD and FOXO4-DBD establish highly heterogeneous interactions. p53-TAD primarily interacts with the N-terminal region of FOXO4-DBD but remains flexible in the complex, nonetheless (Fig. 2b). In fact, p53-TAD may interact with FOXO4-DBD through multiple binding modes, based on our NMR-driven molecular simulations (Fig. 4 and Supplementary Fig. 28).

Although p53-TAD is an inherently unstructured protein domain[15], previous structural studies of p53-TAD complexes with different binding partners have identified disorder-to-order transitions in TAD1 and/or TAD2, regions that form short helical structures upon binding to target proteins[36]. However, our data indicate that p53-TAD and FOXO4-DBD establish dynamic interactions, with p53-TAD remaining highly flexible in the complex and likely adopting interchangeable conformations. These dynamic interactions and interchangeable conformations are supported by the moderate stability of the FOXO4-DBD:p53-TAD complex (Fig. 1e) and by the absence of a secondary structure of p53-TAD based on backbone chemical shifts (Supplementary Fig. 11)[28].

Representative conformers of the FOXO4-DBD:p53-TAD complex highlight inter- and intramolecular contacts consistent with our CSP analysis (Fig. 1a–d). The highest CSP values were observed in residues D48, Q52, W53, and T55 of p53-TAD2, which likely adopts a compact loop conformation when interacting with the N-terminal segment and helices H4 and H3 of FOXO4-DBD. p53-TAD1 also often adopts a

compact loop conformation, which transiently interacts with various parts of FOXO4-DBD, including the C-terminal portion (Supplementary Fig. 28). Although no significant CSPs were observed in this part of FOXO4-DBD, these contacts may explain the reduced flexibility of this domain after p53-TAD binding (Fig. 2a).

Another factor that likely contributes to the plasticity of FOXO4-DBD:p53-TAD interactions is the high flexibility of the N- and C-terminal segments of FOXO4-DBD (residues 86–103 and 186–211, respectively). The N-terminal segment of FOXO4 contains the residues with the largest CSPs (N99, W101 and G102) that interact intermolecularly with various parts of p53-TAD and/or intramolecularly with the helix H4 of FOXO4-DBD (Supplementary Fig. 28) and is thus crucial for p53-TAD binding (Fig. 1a), remaining highly mobile in the complex (Fig. 2a). The various binding modes suggested by our NMR-driven docking simulations differ in these interactions, though; the TAD2 region interacts directly with the N-terminal segment and/or the helix H4 of FOXO4-DBD in some conformers, but not in others. Therefore, the p53-TAD2-binding surface of FOXO4-DBD is primarily formed by the area at the interface of the N-terminal segment, by the N-termini of helices H1 and H3 and by helix H4 (Fig. 4 and Supplementary Fig. 28).

A comparison of the solution structures of FOXO1-, FOXO3-, and FOXO4-DBD has revealed differences in interactions between hydrophobic residues at this interface[37]. These structural differences could explain not only the different binding affinities of individual FOXO-DBDs to p53-TAD but also subtle differences in CSP profiles (Fig. 1). Corroborating these findings, our results also show that the p53- and DNA-binding surfaces of FOXO4-DBD overlap considerably. The N-terminal segment and the region at the interface of helices H1 and H3 of FOXO4-DBD that interact with various regions of p53-TAD also establish nonspecific contacts with the DNA backbone (Fig. 2c and Supplemental Fig. 1b). Consequently, DNA binding inhibits interactions between FOXO4-DBD and p53-TAD, in line with our previous report according to which the formation of the FOXO4:p53 complex blocks p53 binding to DNA but does not affect the DNA-binding properties of FOXO4[28]. The same DNA-mediated displacement of p53-TAD was also observed for FOXO1-DBD and FOXO3-DBD (Supplementary Fig. 16), most likely because the p53-TAD-binding affinities of all three FOXO-DBDs are significantly lower than their DNA-binding affinities, which are in the nM range[38–40]. The exact mechanism of FOXO4/p53-dependent activation of p21 transcription is still unclear, especially considering the FOXO4-mediated inhibition of p53 binding to DNA[28]. Their interaction may increase the local concentration of both transcription factors, thereby stimulating p21 transcription, or modulate the binding of other transcriptional regulators such as p300/CBP and/or the transcriptional machinery[3]. In any event, further studies are needed to clarify this mechanism and the exact role of the interaction between FOXO4 and p53 in DNA binding.

In response to various stress stimuli, p53-TAD is phosphorylated at several residues, likely modulating p53-TAD interactions with some binding partners[18,22,23]. If so, the interaction between p53-TAD and FOXO4-DBD may also be modulated by phosphorylation. This possibility is also implied by the proximity of some phosphorylation sites of p53-TAD to positively charged residues of FOXO4-DBD in their complex (Supplementary Fig. 34) and by the higher binding affinity of the phosphorylation mimicking p53-TAD mutants for FOXO4-DBD (Fig. 5c).

Notwithstanding these advances in our structural understanding of interactions between FOXO4-DBD and p53-TAD, further research is needed to ascertain whether post-translational modifications, especially in p53-TAD, affect interactions between FOXO4 and p53. Furthermore, our study was performed using isolated domains, so these interactions between FOXO4-DBD and p53-TAD may differ in the context of the corresponding full-length proteins. Nevertheless, our CSP profiles of the isolated domains (Fig. 1) are highly similar to those of the longer proteins[28]. This similarity suggests that the binding interface between p53-TAD and FOXO4-DBD is the same in both cases.

In conclusion, p53-TAD and FOXO4-DBD establish highly heterogeneous interactions, with p53-TAD primarily interacting with the N-terminal part of FOXO4-DBD but remaining flexible in the complex. p53-TAD adopts interchangeable conformations, which, together with the flexibility of the N- and C-terminal segments of FOXO4-DBD, enable multiple binding modes. A key part of the p53-binding surface of FOXO4-DBD is the region at the interface of the N-terminal segment, the N-termini of helices H1 and H3, and the helix H4. This region of the FOXO Forkhead domain may be targeted by low molecular weight compounds to modulate transcriptional activity[41,42] and by small peptides to reduce the number of senescent cells, thereby improving tissue homeostasis[4].

Considering their key role in regulating cellular senescence, interactions between p53-TAD and FOXO4-DBD stand out as promising targets in the treatment of aging-associated diseases. Understanding these interactions opens up opportunities for developing specific drug inhibitors aimed at selectively eliminating senescent cells. Such efforts have long been hampered by the lack of structural data. Now, our findings should prompt further research on these interactions and on strategies for their inhibition, with significant translational outputs.

Methods

Protein expression and purification

All FOXO-DBD constructs ($FOXO1_{144-270}$, $FOXO3_{142-267}$, and $FOXO4_{86-211}$) were cloned into the pET-15b vector and expressed as N-terminal $(His)_6$-tagged proteins in Escherichia coli BL21(DE3) cells[28]. The fusion proteins were purified using Chelating-Sepharose Fast Flow (GE Healthcare, Chicago, Illinois, USA) according to a standard protocol. The fusion proteins were eluted using 25 mM Tris-HCl (pH 8.0) buffer containing 500 mM NaCl, 2 mM β-mercaptoethanol and 600 mM imidazole, and the affinity tag was removed using thrombin protease (10 U per 1 mg of fusion protein) during overnight dialysis against 25 mM Tris-HCl (pH 7.5) buffer containing 150 mM NaCl, 1 mM EDTA and 2 mM β-mercaptoethanol. Subsequently, heparin chromatography on a HiTrap Heparin HP column (GE Healthcare, Chicago, Illinois, USA) was performed in 25 mM Tris-HCl (pH 7.5) buffer containing 150 mM NaCl, 1 mM EDTA, and 2 mM DTT. The last purification step was size exclusion chromatography on a Superdex 75 HiLoad column (GE Healthcare, Chicago, Illinois, USA) in 25 mM Tris-HCl (pH 7.5) buffer containing 150 mM NaCl, 1 mM EDTA, 2 mM DTT, and 10 % (w/v) glycerol.

All $p53_{1-93}$ constructs were cloned into the pGEX-6P-1 vector and expressed as N-terminal GST-fusion proteins in Escherichia coli BL21(DE3) cells. The fusion protein was purified using Glutathione Sepharose 4 Fast Flow (GE Healthcare, Chicago, Illinois, USA), and the affinity tag was removed on the column over a 2 h incubation with PreScission protease (10 U per 1 mg of fusion protein). The cleaved protein was eluted in 25 mM Tris-HCl buffer (pH 7.5) containing 500 mM NaCl, 1 mM EDTA, 10 % (w/v) glycerol, and 10 mM DTT. Subsequently, $p53_{1-93}$ proteins were purified by anion exchange on a HiTrap Q column (GE Healthcare, Chicago, Illinois, USA) in 50 mM Tris-HCl buffer (pH 8.0) containing 1 mM EDTA and 2 mM DTT. The last purification step was size exclusion chromatography on a HiLoad Superdex 75 column (GE Healthcare, Chicago, Illinois, USA) and 25 mM Tris-HCl buffer (pH 7.5) containing 150 mM NaCl, 1 mM EDTA, 2 mM DTT, and 10 % (w/v) glycerol.

All ^{15}N isotopically labeled constructs were expressed in minimal media supplemented with 1 g/L of ^{15}N NH_4Cl (Cambridge Isotope Laboratories, Inc., Tewksbury, Massachusetts, USA) as the sole nitrogen source and purified as described above.

Site-specific labeling of single-cysteine mutants

For fluorescence anisotropy (FA) measurements, the $p53_{1\text{-}93}$ A63C single-cysteine mutant were labeled with 5-iodoacetoamidofluorescein (5-IAF) (Sigma-Aldrich s.r.o., St. Louis, Missouri, USA). In 50 mM Tris-HCl (pH 7.5), 100 mM NaCl, and 1 mM EDTA, the protein (50 μM) was mixed with a 40-fold molar excess of 5-IAF. The reaction was incubated overnight at 4 °C in the dark. Excess-free 5-IAF was removed by size exclusion chromatography on a Superdex 75 Increase 10/300 GL column (GE Healthcare, Chicago, Illinois, USA) and 10 mM HEPES buffer (pH 7.5) containing 150 mM NaCl. The percentage of dye incorporation was estimated in light absorption measurements and calculated according to the protocol from Thermo Fisher Scientific. Protein concentration was calculated using the following formula:

$$\text{protein concentration(M)} = \frac{A_{280} - (A_{494} \cdot \text{CF})}{\varepsilon} \quad (1)$$

where ε is a protein extinction coefficient in $M^{-1}cm^{-1}$, using a value of 0.3 as the correction factor (CF). Subsequently, the degree of protein labeling was calculated using the following formula:

$$\text{moles dye per mol protein} = \frac{A_{494}}{\varepsilon' \cdot \text{protein concentration(M)}}. \quad (2)$$

where a value of 68 000 M^{-1} cm^{-1} was used as the extinction coefficient of the dye (ε'). The degree of labeling was ~100 %.

To characterize the interaction between FOXO4-DBD and $p53_{1\text{-}93}$, we designed three $FOXO4_{86\text{-}211}$ single-cysteine mutants (at positions 96, 134, and 162) and four $p53_{1\text{-}93}$ single cysteine mutants (at positions 15, 37, 63, and 90). For PRE NMR measurements, we labeled the single-Cys mutants with paramagnetic MTSSL (Sigma-Aldrich s.r.o., St. Louis, Missouri, USA). All proteins were purified as described above and dialyzed against 50 mM Tris-HCl (pH 7.5) buffer containing 150 mM NaCl and 1 mM EDTA. The PRE probe was dissolved in DMSO to a final concentration of 100 mM and added to the labeling reaction in a 20-fold molar excess over the protein (the protein concentration was 100 − 150 μM). The reaction was incubated for 4 h at room temperature and then overnight at 4 °C, in the dark. Excess-free probe was removed by size exclusion chromatography on a Superdex 75 Increase 10/300 GL column (GE Healthcare, Chicago, Illinois, USA) with 50 mM Tris-HCl (pH 7.5) buffer containing 150 mM NaCl. As shown by MS analysis, labeling was ~100 %.

HSQC NMR titrations

^{1}H-^{15}N HSQC NMR titrations were acquired on a Bruker Avance III™ 600 MHz spectrometer (Bruker, Billerica, Massachusetts, USA) equipped with a $^{13}C/^{1}H/^{15}N$ cryoprobe. All HSQC experiments were measured on 100 μM ^{15}N-labeled protein and binding partner at a given concentration at 298 K in Shigemi NMR tubes (Shigemi Co., LTD, Tokyo, Japan) in 50 mM phosphate buffer (pH 6.5) supplemented with 150 mM NaCl and 5% (v/v) $^{2}H_2O$. The sequence-specific backbone resonance assignments of FOXO1-DBD, FOXO3-DBD, FOXO4-DBD, and p53-TAD were transferred from published data[27,37,43,44]. All spectra were processed in TopSpin software (v3.6) and evaluated in NMRFAM-Sparky software (v3.1)[45]. Derived from 2D ^{1}H-^{15}N HSQC experiments, the CSP values were calculated according to the following formula[46]:

$$\text{CSP} = \sqrt{\left[\Delta\delta_{\text{H}}^2 + \left(\frac{1}{5}\Delta\delta_{\text{N}}\right)^2\right]}. \quad (3)$$

The average relative change in CSP values of selected ^{15}N-labeled p53-TAD residues (S20, W23, K24, L26, V31, S37, M44, L45, D49, and D57) was plotted as a function of FOXO4-DBD concentration and fitted to Eq. 4 [46] to determine K_D values:

$$\text{CSP} = \text{CSP}_{\max}\left\{([p53] + [FOXO4] + K_D) - \left[([p53] + [FOXO4] + K_D)^2 - 4[p53][FOXO4]\right]^{\frac{1}{2}}\right\}/2[p53] \quad (4)$$

where CSP_{max} is the CSP value at saturation, [p53] is the concentration of p53-TAD (20 μM), and [FOXO4] is the concentration of FOXO4-DBD, which ranged from 0 to 1250 μM.

Secondary structure prediction

The experiments for secondary structure prediction were measured on samples containing 100 μM ^{13}C, ^{15}N-labeled protein, and 200 μM binding partner on a Bruker Avance III™ 850 MHz spectrometer (Bruker, Billerica, Massachusetts, USA) equipped with a $^{13}C/^{1}H/^{15}N$ cryoprobe. All experiments were performed in 50 mM phosphate buffer (pH 6.5) containing 150 mM NaCl and 10% (v/v) $^{2}H_2O$ at 298 K in Shigemi NMR tubes (Shigemi Co., LTD, Tokyo, Japan). The secondary structures of p53-TAD and FOXO4-DBD were predicted based on assigned backbone chemical shifts (HN, HA, CA, CB, CO, and N) using TALOS + [47].

PRE measurements

PRE experiments were measured on samples containing 100 μM ^{15}N-labeled protein and 200 μM MTSSL-labeled binding partner on a Bruker Avance III™ 850 MHz spectrometer (Bruker, Billerica, Massachusetts, USA) equipped with a $^{13}C/^{1}H/^{15}N$ cryoprobe. All experiments were performed in 50 mM phosphate buffer (pH 6.5) containing 150 mM NaCl and 10% (v/v) $^{2}H_2O$ at 298 K in Shigemi NMR tubes (Shigemi Co., LTD, Tokyo, Japan). Diamagnetic samples were prepared by adding a 15-fold molar excess of ascorbic acid over the MTSSL-labeled protein to the sample. Intensity ratios I_{para}/I_{dia} were determined in ^{1}H-^{15}N HSQC experiments with a 4 s recovery delay and 16 scans per free induction decay (FID). For measuring ^{1}H transverse relaxation rates, the pulse sequence ¬ji_g2Hn¬ was kindly provided by Dr. Junji Iwahara and previously described by Iwahara et al.[34]. All spectra were processed in TopSpin software (v3.6) and evaluated in NMRFAM-Sparky software (v3.1)[45]. The ^{1}H-Γ_2 rates were calculated in a two-time-point measurement at $\Delta T = 0$ and $\Delta T = 10$ ms by setting the recovery delay to 1 s, with 16 scans per FID, using the following formula:

$$\Gamma_2 = \frac{1}{0.01}\ln\frac{I_{dia}(T = 10\text{ ms}) \cdot I_{para}(T = 0\text{ ms})}{I_{para}(T = 10\text{ ms}) \cdot I_{dia}(T = 0\text{ ms})} \quad (5)$$

^{15}N relaxation measurements

^{15}N relaxation experiments were performed using samples containing 100 μM ^{15}N-labeled protein and 200 μM binding partner on a Bruker Avance III 850 MHz spectrometer (Bruker, Billerica, Massachusetts, USA) equipped with a $^{13}C/^{1}H/^{15}N$ cryoprobe. All experiments were performed in 50 mM phosphate buffer (pH = 6.5) containing 150 mM NaCl and 10% (v/v) $^{2}H_2O$ at 298 K in Shigemi NMR tubes (Shigemi Co., LTD, Tokyo, Japan). Standard Bruker pulse programs for T_1 and T_2 ^{15}N relaxation times were used in NMRlib 2.0[48]. The relaxation delays were 0.0448, 0.0672, 0.112, 0.179, 0.246, 0.381, 0.784, 1.23 s for R_1 and 0, 0.0310, 0.0628, 0.0931, 0.124, 0.186, 0.279 s for R_2 measurements. The recovery delay was set to 1.2 s with 4 or 8 scans per FID. All spectra were processed in TopSpin software (v3.6) and evaluated in NMRFAM-SPARKY software (v3.1)[45]. The rotational correlation time was estimated using the TRACT method[49] as implemented in NMRlib 2.0[48]. In the DNA-addition experiment, FOXO4 consensus DNA containing the DBE motif (sequence: 5′-GACTATGTAAACAACGC-3′) was used at a molar ratio of 1:1. Relaxation data for ^{15}N-labeled p53-TAD, ^{15}N-labeled p53-TAD in the presence of FOXO4-DBD, ^{15}N-labeled FOXO4-DBD, ^{15}N-labeled FOXO4-DBD in the presence of p53-TAD and ^{15}N-labeled p53-TAD in the presence of FOXO4-DBD and DNA have been deposited

in BMRB under accession codes 52703, 52704, 52705, 52706 and 52707.

Distance restrains generation

I_{para}/I_{dia} intensity ratios were converted into distances according to Simon et al.[50] with all constants identical except for proton Larmor frequency (850 MHz), R_2^{dia} (30 s^{-1}), and τ_C (9 ns and 3 ns for FOXO4-DBD and p53-TAD, respectively). As in Battiste and Wagner[51], three classes of distance restraints were used to calculate the structure. Distances between spin-labeled FOXO4-DBD and ^{15}N-labeled p53-TAD were set as follows. Peaks with an intensity ratio < 0.1 were restrained, with no lower bound and with an upper bound of 4 Å. Peaks with an intensity ratio > 0.86 were restrained at the corresponding distance of 22.5 Å, with 4 Å lower and 100 Å upper bounds. Peaks with intensity ratios between 0.1 and 0.85 were restrained at the calculated distance, with 4 Å lower and 7 Å upper bounds. As the actual unpaired electron position was approximated by the CB atom, the upper limit was increased to the maximal distance between the side-chain CB and N in the MTSSL ring (cca 7 Å). For spin-labeled p53-TAD and ^{15}N-labeled FOXO4-DBD, the upper bound was further extended to 10 Å (p53-TAD S15C) and 8 Å (p53-TAD S37C and A63C mutants) to describe the inherent higher chain flexibility of p53-TAD.

High Ambiguity Driven protein-protein DOCKing simulations

To build a HADDOCK 2.4[52] model of the FOXO4-DBD:p53-TAD complex, the Alphafold2 model of $FOXO4_{86\text{-}211}$ was used as the starting structure. To enhance the conformational sampling of p53-TAD, a p53 ensemble was downloaded from the Protein Ensemble Database (entry PED00438)[53]. Residues 1–93 corresponding to p53-TAD were extracted from the deposited models and used as the starting structures of the ligand for the HADDOCK run. In total, 617 distance constraints were calculated from experimental intensity ratios of paramagnetic and diamagnetic samples (I_{para}/I_{dia}, the MTSSL spin label was attached at three positions in FOXO4-DBD and four positions in p53-TAD)[50,54]. In the HADDOCK run, the positions of spin labels were approximated by methionine Cε atom (corresponding in-silico mutants were prepared using Modeler[55]). The resulting starting pool of 1000 structures was subjected to further analysis. An I_{para}/I_{dia} intensity ratios for each conformer were predicted in DEER-PREdict software[54]. Excluding conformers with steric clashes between the modeled MTSSL spin tag and the protein yielded a final data set with 95 conformers. Upon further analysis, sub-ensembles were selected using in-house scripts in R, a programming language for statistical computing and data visualization[56]. The standard Q factor[50]:

$$Q = \sqrt{\frac{\sum\left[\left(\frac{I_{para}}{I_{dia}}\right)_{backcalc} - \left(\frac{I_{para}}{I_{dia}}\right)_{exp}\right]^2}{\sum\left[\left(\frac{I_{para}}{I_{dia}}\right)_{exp}\right]^2}}, \quad (6)$$

where $(I_{para}/I_{dia})_{backcalc}$ and $(I_{para}/I_{dia})_{exp}$ stand for predicted and experimental intensity ratios, respectively, was used to evaluate the agreement between model and experimental intensity profiles. We tested all possible combinations of sub-ensembles with sizes ranging from $N = 2$ (4465 possibilities) to $N = 6$ conformers (869,107,785 possibilities). Except for the ensemble with $N = 2$, the best achievable Q value decreased with the increase in ensemble size. Any sub-ensemble beyond six conformers is impractical, requiring an exhaustive search for all combinations. For this reason, the larger subsets ($N = 10, 13, 16, 20$) were selected using an "incremental" approach, that is, the previous best solution was expanded by combining 3 or 4 new conformers. The plot of Q value vs. ensemble size shows that a plateau is reached at $N = 10$. The final ensemble of FOXO4-DBD:p53-TAD conformers is available in Supplementary Data 1. Starting structures, restraints, and run parameters of the HADDOCK simulation are available in Supplementary Data 2.

Fluorescence anisotropy assay

To determine the binding affinity of FOXO-DBDs towards $p53_{1\text{-}93}$, FOXO1-DBD, FOXO3-DBD, and FOXO4-DBD constructs were designed with the boundaries described above. Using the fluorescein-labeled A63C mutant of $p53_{1\text{-}93}$ as a probe, we performed fluorescence anisotropy (FA) assay in a buffer containing 10 mM HEPES (pH 7.5), 150 mM NaCl, 1 mM TCEP, 0.1% (v/v) Tween 20 and 0.1% (w/v) BSA in a 384-well plate (Corning, USA) using a CLARIO star micro-plate reader (BMG Labtech, Germany). FOXO proteins at a starting concentration of 300 µM and binary dilution series were incubated for 1 h with 50 nM FITC-labeled $p53_{1\text{-}93}$ A63C mutant. The excitation and emission wavelengths were 480 nm and 530 nm, respectively. To determine the K_D value, the data were fitted to the single-site-specific binding model available in GraphPad Prism 8.4.2 (GraphPad Software, La Jolla, CA, USA). All data points are expressed as the mean of three technical replicates.

Reporting summary

Further information on research design is available in the Nature Portfolio Reporting Summary linked to this article.

Data availability

The authors declare that data supporting the findings of this study are available in the main text and its supplementary information files. An ensemble of FOXO4-DBD:p53-TAD conformers is available in Supplementary Data 1. Starting structures, restraints, and run parameters of the HADDOCK simulation are available in Supplementary Data 2. Relaxation data for ^{15}N-labeled p53-TAD, ^{15}N-labeled p53-TAD in the presence of FOXO4-DBD, ^{15}N-labeled FOXO4-DBD, ^{15}N-labeled FOXO4-DBD in the presence of p53-TAD and ^{15}N-labeled p53-TAD in the presence of FOXO4-DBD and DNA have been deposited in BMRB under accession codes 52703, 52704, 52705, 52706 and 52707, respectively. PDB codes of previously published structures used in this study are 3L2C and 1E17. Further information may be requested from the corresponding authors. Source data are provided as a Source Data file. Source data are provided in this paper.

Code availability

The in-house R scripts that were used to analyze and select sub-ensembles have been deposited in Zenodo (https://doi.org/10.5281/zenodo.13838563).

References

1. Wanner, E., Thoppil, H. & Riabowol, K. Senescence and Apoptosis: Architects of Mammalian Development. *Front. Cell Dev. Biol.* **8**, 620089 (2020).
2. Bringold, F. & Serrano, M. Tumor suppressors and oncogenes in cellular senescence. *Exp. Gerontol.* **35**, 317–329 (2000).
3. Bourgeois, B. & Madl, T. Regulation of cellular senescence via the FOXO4-p53 axis. *FEBS Lett.* **592**, 2083–2097 (2018).
4. Baar, M. P. et al. Targeted apoptosis of senescent cells restores tissue homeostasis in response to chemotoxicity and aging. *Cell* **169**, 132–147 (2017).
5. Furuyama, T., Nakazawa, T., Nakano, I. & Mori, N. Identification of the differential distribution patterns of mRNAs and consensus binding sequences for mouse DAF-16 homologues. *Biochem. J.* **349**, 629–634 (2000).
6. Guo, S. et al. Phosphorylation of serine 256 by protein kinase B disrupts transactivation by FKHR and mediates effects of insulin on insulin-like growth factor-binding protein-1 promoter activity through a conserved insulin response sequence. *J. Biol. Chem.* **274**, 17184–17192 (1999).

7. Weigel, D. & Jackle, H. The fork head domain - a novel DNA-binding motif of eukaryotic transcription factors. *Cell* **63**, 455–456 (1990).
8. Hartlmuller, C., Spreitzer, E., Gobl, C., Falsone, F. & Madl, T. NMR characterization of solvent accessibility and transient structure in intrinsically disordered proteins. *J. Biomol. NMR* **73**, 305–317 (2019).
9. de Keizer, P. L. et al. Activation of forkhead box O transcription factors by oncogenic BRAF promotes p21cip1-dependent senescence. *Cancer Res.* **70**, 8526–8536 (2010).
10. Qi, X. F. et al. FoxO3a suppresses the senescence of cardiac microvascular endothelial cells by regulating the ROS-mediated cell cycle. *J. Mol. Cell Cardiol.* **81**, 114–126 (2015).
11. Nogueira, V. et al. Akt determines replicative senescence and oxidative or oncogenic premature senescence and sensitizes cells to oxidative apoptosis. *Cancer Cell* **14**, 458–470 (2008).
12. Obsil, T. & Obsilova, V. Structure/function relationships underlying regulation of FOXO transcription factors. *Oncogene* **27**, 2263–2275 (2008).
13. Fernandez-Fernandez, M. R. & Sot, B. The relevance of protein-protein interactions for p53 function: the CPE contribution. *Protein Eng. Des. Sel.* **24**, 41–51 (2011).
14. Vousden, K. H. & Prives, C. Blinded by the light: The growing complexity of p53. *Cell* **137**, 413–431 (2009).
15. Oldfield, C. J. et al. Flexible nets: disorder and induced fit in the associations of p53 and 14-3-3 with their partners. *BMC Genomics* **9**, S1 (2008).
16. Chang, J., Kim, D. H., Lee, S. W., Choi, K. Y. & Sung, Y. C. Transactivation ability of p53 transcriptional activation domain is directly related to the binding affinity to TATA-binding protein. *J. Biol. Chem.* **270**, 25014–25019 (1995).
17. Teufel, D. P., Freund, S. M., Bycroft, M. & Fersht, A. R. Four domains of p300 each bind tightly to a sequence spanning both transactivation subdomains of p53. *Proc. Natl. Acad. Sci. USA* **104**, 7009–7014 (2007).
18. Feng, H. et al. Structural basis for p300 Taz2-p53 TAD1 binding and modulation by phosphorylation. *Structure* **17**, 202–210 (2009).
19. Raj, N. & Attardi, L. D. The transactivation domains of the p53 protein. *Cold Spring Harb. Perspect. Med.* **7**, https://doi.org/10.1101/cshperspect.a026047 (2017).
20. Kussie, P. H. et al. Structure of the MDM2 oncoprotein bound to the p53 tumor suppressor transactivation domain. *Science* **274**, 948–953 (1996).
21. Lee, C. W., Martinez-Yamout, M. A., Dyson, H. J. & Wright, P. E. Structure of the p53 transactivation domain in complex with the nuclear receptor coactivator binding domain of CREB binding protein. *Biochemistry* **49**, 9964–9971 (2010).
22. Bode, A. M. & Dong, Z. Post-translational modification of p53 in tumorigenesis. *Nat. Rev. Cancer* **4**, 793–805 (2004).
23. Teufel, D. P., Bycroft, M. & Fersht, A. R. Regulation by phosphorylation of the relative affinities of the N-terminal transactivation domains of p53 for p300 domains and Mdm2. *Oncogene* **28**, 2112–2118 (2009).
24. Li, H. H., Li, A. G., Sheppard, H. M. & Liu, X. Phosphorylation on Thr-55 by TAF1 mediates degradation of p53: a role for TAF1 in cell G1 progression. *Mol. Cell* **13**, 867–878 (2004).
25. Shieh, S. Y., Ikeda, M., Taya, Y. & Prives, C. DNA damage-induced phosphorylation of p53 alleviates inhibition by MDM2. *Cell* **91**, 325–334 (1997).
26. Nemoto, S., Fergusson, M. M. & Finkel, T. Nutrient availability regulates SIRT1 through a forkhead-dependent pathway. *Science* **306**, 2105–2108 (2004).
27. Wang, F. et al. Biochemical and structural characterization of an intramolecular interaction in FOXO3a and its binding with p53. *J. Mol. Biol.* **384**, 590–603 (2008).
28. Mandal, R. et al. FOXO4 interacts with p53 TAD and CRD and inhibits its binding to DNA. *Protein Sci.* **31**, e4287 (2022).
29. Kim, J., Ahn, D. & Park, C. J. Biophysical investigation of the dual binding surfaces of human transcription factors FOXO4 and p53. *FEBS J.* **289**, 3163–3182 (2021).
30. Lenard, A. J., Mulder, F. A. A. & Madl, T. Solvent paramagnetic relaxation enhancement as a versatile method for studying structure and dynamics of biomolecular systems. *Prog. Nucl. Magn. Reson Spectrosc.* **132-133**, 113–139 (2022).
31. Madl, T., Guttler, T., Gorlich, D. & Sattler, M. Structural analysis of large protein complexes using solvent paramagnetic relaxation enhancements. *Angew. Chem. Int. Ed. Engl.* **50**, 3993–3997 (2011).
32. Wiedemann, C. et al. Structure and regulatory role of the C-terminal winged helix domain of the archaeal minichromosome maintenance complex. *Nucleic Acids Res.* **43**, 2958–2967 (2015).
33. Tomlinson, J. H., Thompson, G. S., Kalverda, A. P., Zhuravleva, A. & O'Neill, A. J. A target-protection mechanism of antibiotic resistance at atomic resolution: insights into FusB-type fusidic acid resistance. *Sci. Rep.* **6**, 19524 (2016).
34. Iwahara, J., Tang, C. & Marius Clore, G. Practical aspects of (1)H transverse paramagnetic relaxation enhancement measurements on macromolecules. *J. Magn. Reson* **184**, 185–195 (2007).
35. Candau, R. et al. Two tandem and independent sub-activation domains in the amino terminus of p53 require the adaptor complex for activity. *Oncogene* **15**, 807–816 (1997).
36. Dudas, E. F. et al. Tumor-suppressor p53TAD(1-60) forms a fuzzy complex with metastasis-associated S100A4: Structural insights and dynamics by an NMR/MD approach. *Chembiochem* **21**, 3087–3095 (2020).
37. Psenakova, K. et al. Forkhead domains of FOXO transcription factors differ in both overall conformation and dynamics. *Cells* **8**, 966 (2019).
38. Vacha, P. et al. Detailed kinetic analysis of the interaction between the FOXO4-DNA-binding domain and DNA. *Biophys. Chem.* **184C**, 68–78 (2013).
39. Tsai, K. L. et al. Crystal structure of the human FOXO3a-DBD/DNA complex suggests the effects of post-translational modification. *Nucleic Acids Res.* **35**, 6984–6994 (2007).
40. Brent, M. M., Anand, R. & Marmorstein, R. Structural basis for DNA recognition by FoxO1 and its regulation by posttranslational modification. *Structure* **16**, 1407–1416 (2008).
41. Hagenbuchner, J. et al. Modulating FOXO3 transcriptional activity by small, DBD-binding molecules. *Elife* **8**, https://doi.org/10.7554/elife.48876 (2019).
42. Kohoutova, K. et al. Lengthening the guanidine-aryl linker of phenylpyrimidinylguanidines increases their potency as inhibitors of FOXO3-induced gene transcription. *ACS Omega* **7**, 34632–34646 (2022).
43. Weigelt, J., Climent, I., Dahlman-Wright, K. & Wikstrom, M. 1H, 13 C and 15 N resonance assignments of the DNA binding domain of the human forkhead transcription factor AFX. *J. Biomol. NMR* **17**, 181–182 (2000).
44. Wong, T. S. et al. Biophysical characterizations of human mitochondrial transcription factor A and its binding to tumor suppressor p53. *Nucleic Acids Res.* **37**, 6765–6783 (2009).
45. Lee, W., Tonelli, M. & Markley, J. L. NMRFAM-SPARKY: enhanced software for biomolecular NMR spectroscopy. *Bioinformatics* **31**, 1325–1327 (2015).
46. Williamson, M. P. Using chemical shift perturbation to characterise ligand binding. *Prog. Nucl. Magn. Reson. Spectrosc.* **73**, 1–16 (2013).
47. Shen, Y., Delaglio, F., Cornilescu, G. & Bax, A. TALOS + : a hybrid method for predicting protein backbone torsion angles from NMR chemical shifts. *J. Biomol. NMR* **44**, 213–223 (2009).
48. Favier, A. & Brutscher, B. NMRlib: user-friendly pulse sequence tools for Bruker NMR spectrometers. *J. Biomol. NMR* **73**, 199–211 (2019).

49. Lee, D., Hilty, C., Wider, G. & Wuthrich, K. Effective rotational correlation times of proteins from NMR relaxation interference. *J. Magn. Reson* **178**, 72–76 (2006).
50. Simon, B., Madl, T., Mackereth, C. D., Nilges, M. & Sattler, M. An efficient protocol for NMR-spectroscopy-based structure determination of protein complexes in solution. *Angew. Chem. Int. Ed. Engl.* **49**, 1967–1970 (2010).
51. Battiste, J. L. & Wagner, G. Utilization of site-directed spin labeling and high-resolution heteronuclear nuclear magnetic resonance for global fold determination of large proteins with limited nuclear overhauser effect data. *Biochemistry* **39**, 5355–5365 (2000).
52. van Zundert, G. C. P. et al. The HADDOCK2.2 web server: User-friendly integrative modeling of biomolecular complexes. *J. Mol. Biol.* **428**, 720–725 (2016).
53. Lazar, T. et al. PED in 2021: a major update of the protein ensemble database for intrinsically disordered proteins. *Nucleic Acids Res.* **49**, D404–D411 (2021).
54. Tesei, G. et al. DEER-PREdict: Software for efficient calculation of spin-labeling EPR and NMR data from conformational ensembles. *PLoS Comput. Biol.* **17**, e1008551 (2021).
55. Webb, B. & Sali, A. Comparative Protein Structure Modeling Using MODELLER. *Curr. Protoc. Protein Sci.* **86**, 2 9 1–2 9 37 (2016).
56. Srb, P. & Veverka, V. Zenodo. https://doi.org/10.5281/zenodo.13838563 (2024).

Acknowledgements

This study was supported by Czech Science Foundation (grant number 21-02080S, T.O.), the Grant Agency of the Charles University (grant number 296621, K.K.), the Czech Academy of Sciences (RVO: 67985823 of the Institute of Physiology, V.O.) and by project National Institute for Cancer Research (Program EXCELES, ID Project No. LX22NPO5102, V.V.) - Funded by the European Union - Next Generation EU. We thank Carlos V. Melo for editing the article.

Author contributions

T.O., V.V., and V.O. supervised the project and provided scientific guidance. K.K. performed protein expression/purification experiments, NMR experiments, and FA measurements. P.S. performed NMR experiments and molecular modeling. K.K., V.O., and T.O. wrote the manuscript. All co-authors revised the manuscript.

Competing interests

The authors declare no competing interests.

Additional information

Supplementary information The online version contains supplementary material available at https://doi.org/10.1038/s41467-025-59106-5.

Correspondence and requests for materials should be addressed to Veronika Obsilova, Vaclav Veverka or Tomas Obsil.

Peer review information *Nature Communications* thanks the anonymous reviewers for their contribution to the peer review of this work. A peer review file is available.